

## Pulsed EPR/ENDOR Characterization of the Cu<sup>2+</sup> Surface Site in Photosynthetic Bacterial Reaction Centers

L. M. Utschig,<sup>\*,†</sup> A. V. Astashkin,<sup>‡</sup> A. M. Raitsimring,<sup>‡</sup> M. C. Thurnauer,<sup>†</sup> and O. G. Poluektov<sup>†</sup>

Chemistry Division, Argonne National Laboratory, Argonne, Illinois 60439, and  
Department of Chemistry, University of Arizona, Tucson, Arizona 85721

Received: December 5, 2003; In Final Form: April 5, 2004

X-band pulsed electron paramagnetic resonance was used to elucidate details of the Cu<sup>2+</sup> surface binding site involved in Q<sub>A</sub><sup>−</sup>Q<sub>B</sub> → Q<sub>A</sub>Q<sub>B</sub><sup>−</sup> electron transfer in photosynthetic bacterial reaction centers (RCs). Electron spin-echo envelope modulation (ESEEM) spectroscopy was employed to measure the hyperfine and electric quadrupole interactions of weakly coupled <sup>14</sup>N nuclei, and X-band pulsed electron nuclear double resonance (ENDOR) spectroscopy was used to probe strongly coupled <sup>14</sup>N nuclei. The <sup>14</sup>N ESEEM observed for Cu<sup>2+</sup> at the surface site of RCs results from a single histidine ligand. In addition, the ENDOR spectra reveal the presence of one more nitrogen ligand in the Cu<sup>2+</sup> coordination sphere that we tentatively assign as a peptide backbone nitrogen. The similarity of the ESEEM and ENDOR spectra for RCs from *Rb. sphaeroides*, *Rb. capsulatus*, and *Blc. viridis* suggests a universal intrinsic structural site. These results indicate that Cu<sup>2+</sup> has a different coordination environment from the crystallographically characterized Zn<sup>2+</sup> and Cd<sup>2+</sup> surface sites in *Rb. sphaeroides* RCs. These structural differences may be associated with observed metal ion specific differences in alteration of Q<sub>A</sub><sup>−</sup>Q<sub>B</sub> → Q<sub>A</sub>Q<sub>B</sub><sup>−</sup> electron transfer.

### 1. Introduction

The photosynthetic conversion of light into useful chemical energy involves rapid, sequential electron transfer resulting in charge separation. In photosynthetic bacteria, these light-initiated reactions occur in integral membrane proteins called reaction centers (RCs). The generalized function of the protein is to intricately anchor redox cofactors at specific distances and orientations, thereby facilitating efficient electron transfer. The experimental challenge is to establish the specific function and important characteristics of localized, anisotropic polypeptide environments involved in photosynthetic charge separation. The structurally characterized bacterial RC<sup>1–3</sup> consists of three 30–35 kDa protein subunits, the two transmembrane pigment-containing subunits L and M and the cytoplasmic hydrophilic H-subunit. Buried within the protein matrix are one high-spin iron(II) and eight chromophores, including four bacteriochlorophylls (BChl), two bacteriopheophytins (Bph), and two quinones (Q). Following photoexcitation of a bacteriochlorophyll dimer (P), the electron is transferred through one set of cofactors terminating in the electron transfer between two quinones, Q<sub>A</sub> and Q<sub>B</sub>.

The electron transfer between Q<sub>A</sub> and Q<sub>B</sub> is temperature activated,<sup>4–6</sup> coupled to proton movement,<sup>7,8</sup> believed to be rate-limited by protein motion,<sup>9–11</sup> and modulated by metal ions.<sup>12,13</sup> For example, isolated RCs were found to bind Zn<sup>2+</sup> stoichiometrically and in a site distinct from the non-heme high-spin Fe<sup>2+</sup> site, which is buried in the protein interior between Q<sub>A</sub> and Q<sub>B</sub>.<sup>12</sup> When Zn<sup>2+</sup> is bound to this site, electron transfer between the quinones Q<sub>A</sub> and Q<sub>B</sub> is slowed and the room-

temperature kinetics become distributed across the microsecond to millisecond time range.<sup>12</sup> Furthermore, metal binding influences the proton uptake by Q<sub>B</sub> in both isolated<sup>13</sup> and membrane-bound RCs.<sup>14</sup> Other metal ions, including Cd<sup>2+</sup>, Ni<sup>2+</sup>, and Cu<sup>2+</sup> have been shown to have slightly different effects on electron transfer and proton uptake.<sup>12,13,15–17</sup> Correlating these effects with the metal site structures will be important for understanding the allosteric modulation of electron and proton transfer.

The locations of the Zn<sup>2+</sup> and Cd<sup>2+</sup> metal binding sites have been determined by X-ray diffraction of *Rb. sphaeroides* RC crystals soaked in solutions containing excess metal ion.<sup>18</sup> Both metal ions bind to the same site near the surface of the protein, 18 Å away from Q<sub>B</sub>, coordinating to three protein ligands, two histidines and one aspartate acid residue. Similar to Zn<sup>2+</sup>, Cu<sup>2+</sup> (3d<sup>9</sup>) binds specifically and stoichiometrically to the RC surface.<sup>19</sup> While the Zn<sup>2+</sup> and Cd<sup>2+</sup> metal binding sites have been determined by X-ray diffraction, and preliminary X-ray results are also available for Co<sup>2+</sup> and Ni<sup>2+</sup>,<sup>18</sup> the surface Cu<sup>2+</sup> site structure has been studied in solution with continuous wave (CW) and pulsed electron paramagnetic resonance (EPR) spectroscopy. These studies provided evidence that RCs isolated from *Rb. sphaeroides*, *Rb. capsulatus*, and *Blc. viridis* have surface Cu<sup>2+</sup> binding sites involved in electron transfer<sup>15</sup> and implicated histidine amino acid side chains as ligands to the Cu<sup>2+</sup>.<sup>19</sup>

Herein, we have applied electron spin-echo envelope modulation (ESEEM) and pulsed electron-nuclear double resonance (ENDOR) spectroscopic techniques to further delineate structural details of the surface Cu<sup>2+</sup> sites of RCs from *Rb. sphaeroides*, *Rb. capsulatus*, and *Blc. viridis*. Specifically, we were interested in the number of histidine ligands and in identifying other possible ligands at the Cu<sup>2+</sup> site. This work demonstrates both the similarity of Cu<sup>2+</sup> site structure for different species and differences of the solution Cu<sup>2+</sup> site

\* Corresponding author. Telephone: (630) 252-3544. Fax: (630) 252-9289. E-mail: utschig@anl.gov.

<sup>†</sup> Argonne National Laboratory.

<sup>‡</sup> University of Arizona.

structure from the crystallographically determined metal sites of Zn<sup>2+</sup>, Cd<sup>2+</sup>, Co<sup>2+</sup>, and Ni<sup>2+</sup> *Rb. sphaeroides* RC derivatives.

## 2. Materials and Methods

RCs from *Blc. viridis*,<sup>20</sup> *Rb. capsulatus*,<sup>15,21</sup> and *Rb. sphaeroides*<sup>22</sup> were isolated and purified as previously described. Stoichiometric Cu–RC complexes were prepared by gel-filtration procedures as previously detailed,<sup>15,19</sup> and the basic procedure is outlined here. RC protein in 10 mM HEPES pH 7.9, 10–20 mM NaCl, and 0.045% lauryldimethylamine *N*-oxide (LDAO) was incubated with 2–10 equiv of CuSO<sub>4</sub> at ice temperature for several hours. Free Cu<sup>2+</sup> was separated from bound metal ion by gel-filtration chromatography through a Sephadex G-25 (Pharmacia) column. Inductively coupled plasma–atomic emission spectroscopy (ICP–AES) on a Thermo Jarell Ash Atomscan Advantage spectrometer was used to determine the amount of Cu bound to the RC. For the samples in this study, the Cu/Fe/RC ratios determined by this method were 0.9 Cu/0.9 Fe/RC for *Rb. sphaeroides* RCs, 1.3 Cu/1.2 Fe/RC for *Rb. capsulatus* RCs, and 1.0 Cu/5 Fe/RC for *Blc. viridis* RCs. Centriprep-50 (Amicon) devices were used to concentrate the RCs. EPR samples were dark-adapted, frozen, and stored in liquid N<sub>2</sub>.

ESEEM and ENDOR measurements were performed on a home-built pulsed EPR spectrometer operating in the microwave (mw) frequency range from 8 to 18 GHz (X- and K<sub>u</sub>-bands) and equipped with a helium-flow cryostat (Oxford CF935) and a pulsed ENDOR accessory. The cylindrical dielectric ENDOR resonator was described earlier.<sup>23</sup> The radio frequency (rf) amplifier AR-250L (Amplifier Research) provided a nominal output power of about 1 kW in the pulsed mode. The measurement temperature was about 8 K.

The simulations of the ESEEM and ENDOR spectra have been performed for the  $B_0$  values corresponding to the maximum of the ESE field sweep (near  $g_{\perp}$ ). A combination of two factors—coaxiality of the  $\mathbf{g}$ -tensor and the Cu<sup>2+</sup> hyperfine interaction (hfi) tensors, and a rather large Cu<sup>2+</sup> hfi component  $A_{\parallel}$  (~164 G for *Rb. sphaeroides*)<sup>15</sup>—result in a very useful property of this particular spectral position. That is, at X-band, the EPR signals corresponding to  $g_{\parallel}$  (at  $m_I = 3/2$ ) and  $g_{\perp}$  overlap, and the ESEEM and ENDOR spectra recorded at (nominally)  $g_{\perp}$  become practically indistinguishable from those of an orientationally disordered system with an isotropic  $g$ -factor. Importantly, these spectra are virtually insensitive to the orientations of the ligand hfi and nuclear quadrupole interaction (nqi) tensors relative to the  $g$ -frame. Since in this work we were not interested in the above orientational parameters, we performed our simulations with full orientational averaging and without orientational selection.

The simulations with distributed parameters were performed in the following way. The distributed parameters were varied stepwise, and for each realization of the parameters the ESEEM was calculated. This ESEEM was then multiplied by the statistical weight of the given realization (which in our case is a product of Gaussian statistical weights of each of the distributed parameters) and added to the ESEEM accumulated at the previous steps. The ENDOR simulations with distributed parameters were performed in the same way.

## 3. Results and Discussion

**3.1. <sup>14</sup>N ESEEM.** Earlier ESEEM measurements<sup>15,19</sup> revealed the presence of <sup>14</sup>N-containing ligands in the coordination sphere of the surface Cu<sup>2+</sup> site in bacterial RCs. With this technique, one observes periodicities (modulations) in the ESE signal

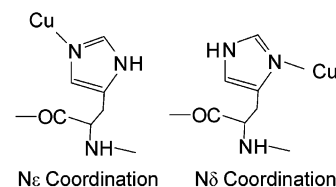


**Figure 1.** Schematic representation of Ne and Nd coordination of histidine to copper. Note that the position of the imino N (directly coordinated nitrogen, observed with ENDOR) vs. the amino N (“remote” nitrogen, observed with ESEEM) on the imidazole changes depending on Cu<sup>2+</sup> coordination.

amplitude that arise from the interaction of the unpaired electron spin of Cu<sup>2+</sup> with magnetic nuclei. In particular, in the case of a histidine coordination, the ESEEM is caused by the interaction with the so-called remote nitrogens (i.e., those imidazole nitrogens that are not coordinated to Cu<sup>2+</sup>; see Figure 1).<sup>24</sup>

The nuclear quadrupole interaction (nqi) parameters of the <sup>14</sup>N nuclei at the Cu<sup>2+</sup> site estimated from simple analysis of the <sup>14</sup>N ESEEM spectra were typical for the imidazole amino group, showing that one type of ligand to the surface Cu<sup>2+</sup> was histidine. The number of the histidine ligands, however, was not determined. Therefore, in this work we repeated the three-pulse ESEEM experiments, obtained two-dimensional (2D) hyperfine sublevel correlation (HYSCORE) spectra, and performed numerical simulations of the <sup>14</sup>N ESEEM data in order to obtain the hfi and nqi parameters of the remote imidazole amino nitrogen(s) more accurately, and to determine the number of coordinated histidine residues.

As an example, Figure 2 shows the stimulated <sup>14</sup>N ESEEM spectra recorded at the magnetic fields corresponding to the maximum of the ESE signal for Cu<sup>2+</sup> bound to the surface sites of *Rb. sphaeroides*, *Rb. capsulatus*, and *Blc. viridis* RCs. These ESEEM spectra are characteristic of a nitrogen nucleus for the condition where the Zeeman and hyperfine interactions almost cancel each other in one of the electron spin manifolds. Theoretically four lines should be observed in such spectra.<sup>25</sup> The three “pure quadrupole” lines of the nitrogen transitions within the electron spin manifold where the Zeeman/hyperfine cancellation takes place have frequencies

$$\nu_0 = 2k\eta; \quad \nu_- = k(3 - \eta); \quad \nu_+ = k(3 + \eta) \quad (1)$$

where  $k = e^2Qq/4h$  ( $e$  is the electron charge,  $Q$  is the quadrupole moment of the nucleus,  $q$  is the largest component of the electron field gradient tensor on the nucleus, and  $h$  is Planck’s constant) and  $\eta$  is the asymmetry parameter of the electric field gradient on the nucleus. The other electron spin manifold will be represented in the ESEEM spectra by the so-called “double quantum transition” line that corresponds to the  $\Delta m = 2$  transition of <sup>14</sup>N and is located at

$$\nu_{\Delta m=2} \approx 2[(\nu_N + A/2)^2 + k^2(3 + \eta^2)]^{1/2} \quad (2)$$

In this expression  $\nu_N$  is the Zeeman frequency of <sup>14</sup>N and  $A$  is the effective hfi constant:  $A = a_{\text{iso}} + T_{ZZ}$ , where  $a_{\text{iso}}$  is the isotropic hfi constant and  $T_{ZZ}$  is the secular component of the anisotropic hfi. The two “single quantum transition” lines that belong to this manifold are usually too broad to be observed.

In the experimental spectra, the triplet of “pure quadrupole” lines located at low frequencies ( $\nu \leq 1.5$  MHz) is poorly resolved. This indicates that the cancellation condition is not perfectly satisfied. Still, from the positions of the high-frequency ( $\nu_+ \sim 1.5$  MHz) and low-frequency ( $\nu_0 \sim 0.6$  MHz) lines in this triplet, we can estimate  $k \approx 0.4$  MHz and  $\eta \approx 0.8$ . Such

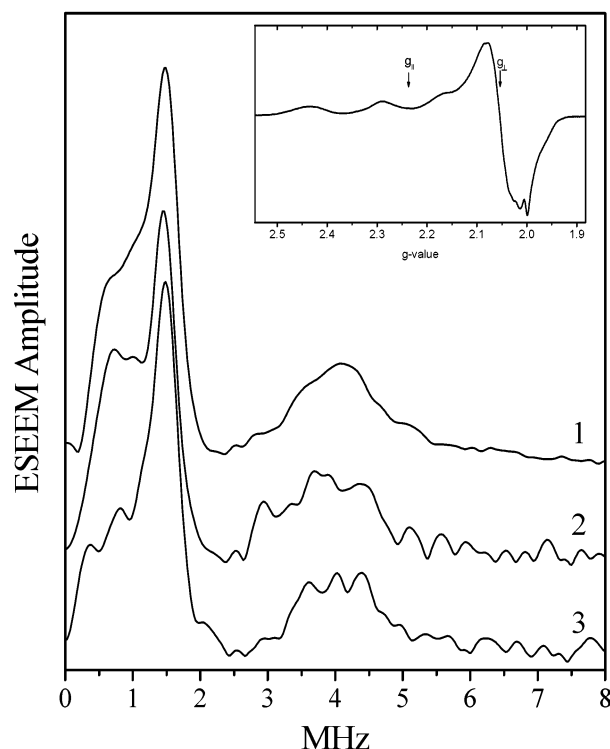


**Figure 2.** Stimulated ESEEM spectra of surface  $\text{Cu}^{2+}$  centers in *Rb. sphaeroides* (trace 1), *Blc. viridis* (trace 2), and *Rb. capsulatus* (trace 3) obtained at  $g_{\perp}$  turning points of the EPR spectra. Trace 1 is obtained at  $B_0 = 3255$  G and the microwave (mw) frequency  $\nu_{\text{mw}} = 9.4384$  GHz. Trace 2 is obtained at  $B_0 = 3265$  G and  $\nu_{\text{mw}} = 9.460$  GHz. Trace 3 is obtained at  $B_0 = 3260$  G and  $\nu_{\text{mw}} = 9.4487$  GHz. Time interval between the first and second mw pulses,  $\tau = 400$  ns; mw pulses  $= 3 \times 10$  ns. Inset: X-band (9.14 GHz) CW EPR spectrum of  $\text{Cu}^{2+}$  bound to surface of *Rb. sphaeroides* RCs. The spectrum is typical for type II  $\text{Cu}^{2+}$  centers in proteins. The data were collected in the dark at 12 K with 20 G modulation amplitude, 2 mW microwave power, and 100 kHz modulation frequency.

nqi parameters are very close to those of the amino nitrogen in the imidazole ring of histidine,<sup>26</sup> and are similar to those observed for other proteins that are known to exhibit copper coordination by histidines.<sup>27–32</sup> The maximum of the  $\nu_{\Delta m=2}$  line is located at the frequency of about 4 MHz, which gives  $A \sim 1.7$  MHz. The separate contributions to  $A$  of the isotropic and anisotropic hfi constants can be established with the aid of numerical simulations.

In addition to the stimulated ESEEM, we have also performed HYSORE experiments because the relative intensities of the correlation lines in HYSORE spectra are sensitive to the relative orientation of the hfi and nqi tensors. The HYSORE spectra show the  $^{14}\text{N}$  lines in the  $(++)$  quadrant only (see, e.g., Figure 3a), while in the  $(-+)$  quadrant no appreciable intensity is observed. The main off-diagonal  $^{14}\text{N}$  features in the  $(++)$  quadrant are the  $(\nu_+, \nu_{\Delta m=2})$  and  $(\nu_{\Delta m=2}, \nu_+)$  correlation lines located at the frequencies of about (1.5, 4) and (4, 1.5) MHz, respectively. Therefore, in the ESEEM simulations, the orientation between the hfi and nqi tensors should be selected in such a way as to result in dominating  $(\nu_+, \nu_{\Delta m=2})$  and  $(\nu_{\Delta m=2}, \nu_+)$  HYSORE correlation lines. On the other hand, the lines in the HYSORE spectrum situated along the main diagonal are not usually simulated because they have strong contributions from three-pulse (stimulated) ESEEM.

Numerical simulations (see Materials and Methods) have shown that the observed nitrogen ESEEM results from a single  $^{14}\text{N}$  nucleus with  $a_{\text{iso}} \approx 1.3$  MHz and the anisotropic hfi tensor  $(T_{11}, T_{22}, T_{33}) \approx (0.5, 0.25, -0.75)$  MHz. In addition, a broad

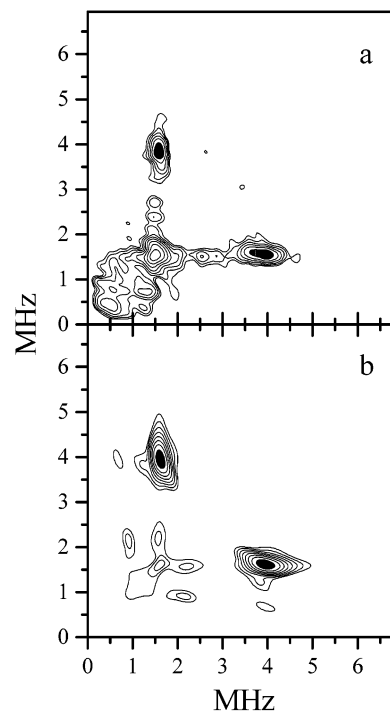


**Figure 3.** (a) HYSORE spectrum of surface  $\text{Cu}^{2+}$  centers in *Rb. sphaeroides* obtained at  $g_{\perp}$  turning point of the EPR spectrum. Experimental conditions:  $\nu_{\text{mw}} = 9.4384$  GHz;  $B_0 = 3255$  G; mw pulses  $= 4 \times 10$  ns;  $\tau = 350$  ns. (b) HYSORE spectrum simulated for a single imidazole amino  $^{14}\text{N}$  nucleus with  $a_{\text{iso}} = 1.3$  MHz, anisotropic hfi tensor  $(T_{11}, T_{22}, T_{33}) = (0.5, 0.25, -0.75)$  MHz,  $k = 0.396$  MHz, and  $\eta = 0.8$ . In addition,  $a_{\text{iso}}$  and  $\eta$  were Gaussian distributed around the central values given above, with the widths between the maximal slope points of 0.45 MHz and 0.3, respectively. The orientation of the nqi tensor with respect to the hfi tensor was defined by the Euler angles  $\varphi = 90^\circ$ ,  $\theta = 60^\circ$ , and  $\psi = 90^\circ$  (see text for definitions).

statistical distribution of  $a_{\text{iso}}$  was required to explain the large width of the double quantum line (see Figure 3b caption for the full list of simulation parameters). The nqi coupling constant was found to be  $k \approx 0.396$  MHz, and the average asymmetry parameter that resulted from the simulations was the same as that estimated above,  $\eta \approx 0.8$ . The orientation of the nqi tensor frame ( $\mathbf{xyz}$ ) with respect to the hfi tensor frame ( $\mathbf{123}$ ) was defined by Euler angles  $\varphi = 90^\circ$ ,  $\theta = 60^\circ$ , and  $\psi = 90^\circ$ , which are the angles for three consecutive rotations around, respectively,  $\mathbf{x}$ , newly obtained  $\mathbf{y}$ , and newly obtained  $\mathbf{z}$ . The situation with all of the angles equal to zero corresponds to the orientation of  $\mathbf{x} \parallel \mathbf{1}$ ,  $\mathbf{y} \parallel \mathbf{2}$ , and  $\mathbf{z} \parallel \mathbf{3}$ . Examples of simulations with the described parameters are shown in Figures 3b and 4.

The absolute values of our simulated anisotropic hfi tensor components are considerably greater than a simple point dipole estimate ( $|T_{\perp}| \sim 0.07$  MHz) that can be obtained based on the Cu–nitrogen distance of about 4.2 Å.<sup>33</sup> This observation is in qualitative agreement with the results of earlier studies of Cu–imidazole complexes,<sup>24,34,35</sup> and it indicates that the anisotropic hfi of the imidazole amino nitrogen is mostly determined by the spin density delocalized in the imidazole ring.

**3.2. ENDOR of Strongly Coupled  $^{14}\text{N}$ .** While ESEEM spectra are sensitive to magnetic nuclei with weak hfi, the strongly coupled nuclei (e.g., the imino nitrogens of the coordinated histidine) can be observed using pulsed ENDOR spectroscopy. Figure 5 shows Davies ENDOR spectra of the  $\text{Cu}^{2+}$  surface site of RCs from *Rb. sphaeroides* (traces 1–4) and *Blc. viridis* (trace 5) obtained at different magnetic fields using the microwave pulses of 30 (180°), 15 (90°), and 30 ns (180°) duration. These spectra are typical for strongly coupled,



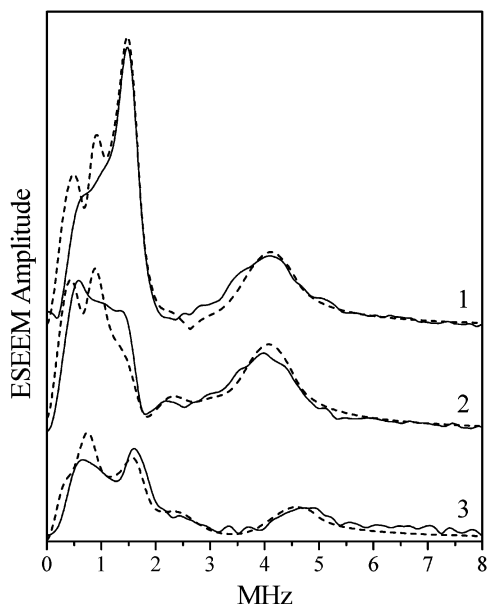


**Figure 4.** Solid lines: stimulated ESEEM spectra of surface Cu<sup>2+</sup> centers in *Rb. sphaeroides* obtained at  $g_{\perp}$  turning point of the EPR spectrum. Traces 1 and 2 are obtained at  $B_0 = 3255$  G and  $\nu_{mw} = 9.4384$  GHz, while trace 3 is obtained at  $B_0 = 3910$  G and  $\nu_{mw} = 11.30$  GHz. Time interval between the first and second mw pulses,  $\tau$ , is 400 ns for traces 1 and 3 and 260 ns for trace 2; mw pulses =  $3 \times 10$  ns. Dashed lines are simulations for a single imidazole amino <sup>14</sup>N nucleus with parameters given in the caption for Figure 3b.

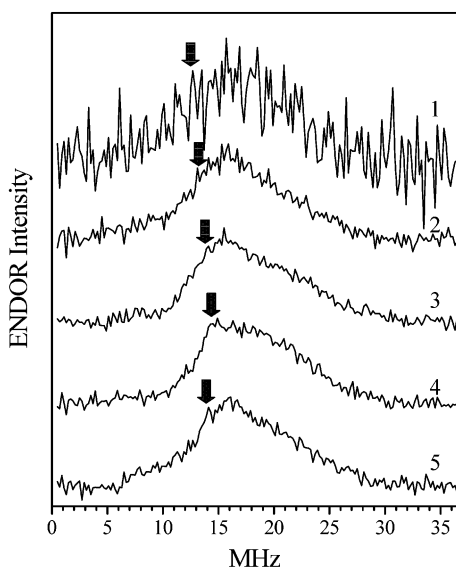


**Figure 5.** Davies ENDOR spectra of surface Cu<sup>2+</sup> centers in *Rb. sphaeroides* (traces 1–4) and *Blc. viridis* (trace 5). Traces 1–4 are recorded at  $B_0 = 2920, 3120, 3255,$  and  $3350$  G, respectively, and  $\nu_{mw} = 9.4384$  GHz. Trace 5 is recorded at  $B_0 = 3265$  G and  $\nu_{mw} = 9.460$  GHz. Other experimental conditions: mw pulses =  $30$  ( $180^\circ$ ),  $15$  ( $90^\circ$ ), and  $30$  ns ( $180^\circ$ ). Time interval between the first and second mw pulses,  $T = 20$   $\mu$ s. Time interval between the second and third mw pulses,  $\tau = 380$  ns. rf pulse duration,  $5$   $\mu$ s.

directly bound <sup>14</sup>N ligands to Cu<sup>2+</sup>.<sup>36,37</sup> The lines of weakly coupled protons from the protein and ligands are not discernible in these spectra because of the very short duration of the microwave pulses<sup>38</sup> (arrows in Figure 5 indicate calculated positions of the proton matrix line). The <sup>14</sup>N lines are rather featureless and span the frequency range from about 10 MHz to about 30 MHz. The shape of the spectrum changes very little with the magnetic field position in the EPR spectrum.

To explain the ENDOR spectra of Figure 5, we have to consider the relevant theoretical and experimental information available in the literature. To the first order in hfi and nqi the positions of the ENDOR lines of strongly coupled <sup>14</sup>N ligands are described by

$$\nu = |A/2| \pm \nu_N \pm P \quad (3)$$

where  $A$  and  $P$  are the secular components of the hfi and nqi, respectively. The two consecutive additions/subtractions are independent of one another, which results in four transition lines centered around  $\nu = |A/2|$ .

Let us consider the hfi term first. With an axial hfi tensor (which is a good approximation in this case) the secular hfi component is given by

$$A = a_{iso} + T_{\perp}(1 - 3 \cos^2 \theta_{hB}) \quad (4)$$

where  $\theta_{hB}$  is the angle between the main hfi axis and the direction of the magnetic field,  $B_0$ . The values of  $a_{iso}$  and  $T_{\perp}$  are mostly determined by the hybridization of the bonding nitrogen orbital and by the spin density  $\rho_N$  delocalized on this orbital from the central Cu<sup>2+</sup> ion. For a hybrid orbital being a mixture of 2p and 2s orbitals the isotropic hfi constant is approximately equal to

$$a_{iso} \approx [a_s c_s + a_p(1 - c_s)]\rho_N \quad (5)$$

where  $a_s \approx 1540$  MHz<sup>39</sup> is the isotropic hfi constant that would be observed if the whole spin density were localized on the nitrogen 2s orbital,  $a_p \approx 50$  MHz<sup>39</sup> is the isotropic hfi constant that would be observed if the whole spin density were localized on the nitrogen 2p orbital, and  $c_s$  is the s-character of the hybrid orbital equal to 1/4, 1/3, and 1/2 for  $sp^3$ ,  $sp^2$  and  $sp$  orbitals, respectively. For the  $sp^3$ ,  $sp^2$ , and  $sp$  hybrid orbitals the second term in parentheses in eq 5 is about 1 order of magnitude smaller than the first one and can be neglected.

Equation 5 predicts a correlation between the hybridization and the hfi constant of the nitrogen ligand. Indeed, such a correlation was observed in a systematic study by Iwaizumi et al.<sup>40</sup> that has shown that typical values of  $a_{iso}$  for nitrogens with  $sp^2$  hybridization are about 40 MHz while those for nitrogens with  $sp^3$  hybridization are about 30 MHz. The average typical spin density  $\rho_N$  estimated from these values is about 7.2%.

The anisotropic hfi constant can be approximately represented as a sum of two terms:

$$T_{\perp} \approx -\frac{g\beta g_n \beta_n}{R_{CuN}} \rho_{Cu} + T_p(1 - c_s)\rho_N \quad (6)$$

where  $g$  and  $g_n$  are, respectively, the electronic and nuclear  $g$ -factors,  $\beta$  is the Bohr magneton,  $\beta_n$  is the nuclear magneton,  $R_{CuN}$  is the distance between Cu<sup>2+</sup> and <sup>14</sup>N ligand nucleus,  $\rho_{Cu}$  is the spin density on Cu<sup>2+</sup>, and  $T_p \approx -50$  MHz<sup>39</sup> is the value of  $T_{\perp}$  that would be observed if the whole spin density were localized on a 2p orbital of <sup>14</sup>N. For four-coordinated Cu<sup>2+</sup> with nitrogen and oxygen ligands the value of  $\rho_{Cu}$  may be roughly estimated to be about 0.7–0.8 (because about 7% of spin density may be transferred to each nitrogen ligand (see above) and about 5% can be transferred to each oxygen ligand<sup>41</sup>). With  $R_{CuN} \approx 2$ – $2.1$  Å, the first term in eq 6 is about  $-0.5$  MHz. The second term is considerably greater and is between  $-2$  and  $-3$  MHz, depending on hybridization. Therefore, the total  $T_{\perp} \approx -3$  MHz can be taken as a good average estimate of the anisotropic hfi constant for <sup>14</sup>N ligands.

Finally, we have to consider the  $nq_i$  term. In the discussion that follows, we are interested in the imino nitrogen of histidine and a peptide nitrogen as possible ligands to  $\text{Cu}^{2+}$  in the bacterial RCs. The quadrupole coupling constants,  $e^2Qq/h$ , are equal to about  $3.3 \pm 0.3$  MHz for both uncoordinated histidine (imidazole) imino  $^{14}\text{N}$  and peptide  $^{14}\text{N}$ .<sup>26</sup> Upon coordination, the population of the lone pair orbital decreases, leading to significant reduction of quadrupole coupling constants, down to the values on the order of 2 MHz for imino  $^{14}\text{N}$ <sup>42</sup> and 1.5 MHz for peptide  $^{14}\text{N}$ .<sup>43</sup> The asymmetry parameter,  $\eta$ , of the electric field gradient tensor for the imino  $^{14}\text{N}$  of histidine increases dramatically, from about 0.1 to about 0.5–0.7,<sup>42</sup> while for peptide  $^{14}\text{N}$  it increases only slightly, from about 0.5 to about  $0.75 \pm 0.25$ .<sup>43</sup>

As follows from the ESEEM results discussed above, one of the ligands to the surface  $\text{Cu}^{2+}$  center in the studied bacterial RCs is histidine. A survey of the relevant literature shows that the ENDOR lines of the histidine imino nitrogen that is directly coordinated to  $\text{Cu}^{2+}$  and lies in the plane of its  $d_{x^2-y^2}$  orbital typically form a single broad feature that occupies the frequency range between 18 and 30 MHz,<sup>36,44</sup> which corresponds to hfi constants of about 40–50 MHz typical for  $sp^2$ -hybridized  $^{14}\text{N}$ , as discussed above. If the complex geometry is distorted and this nitrogen lies out of the plane of the  $\text{Cu}^{2+}$   $d_{x^2-y^2}$  orbital, the hyperfine constant can be significantly smaller, and the corresponding ENDOR lines can be shifted to lower frequencies. This effect was observed in the ENDOR spectra of blue copper proteins, where one of the histidine nitrogens gave the ENDOR line(s) in the usual frequency range above 18 MHz, while the other one resonated at the frequencies of about 10 MHz.<sup>44</sup>

In our ENDOR spectra the upper limit of the  $^{14}\text{N}$  resonances is located at about 30 MHz, and in view of the ESEEM results discussed above, the high-frequency part of the spectrum is readily assignable to the imino nitrogen of equatorially coordinated histidine. The part of the spectrum below 18 MHz, however, should be attributed to a nitrogen ligand with significantly smaller hfi constants. As follows from the theoretical discussion and experimental data mentioned above, this second ligand could be assigned as another histidine, whose position departs from an exact equatorial one. Another option would be to assign this ligand as  $sp^3$ -hybridized  $^{14}\text{N}$ , the most likely candidate being peptide nitrogen.

Figure 6 shows that the experimental ENDOR spectral shape can be approximately reproduced if one histidine nitrogen and one peptide nitrogen are included in the simulation (actually, such simulations only allow one to estimate the relative number of nuclei, but since we already know from ESEEM that there is a single “normal” histidine ligand, we conclude that there is a single peptide ligand). To reproduce the smooth featureless experimental spectral shape, the isotropic hfi constants had to be distributed within broad limits.

Because of this broad hfi distribution, the simulation is actually insensitive to the  $nq_i$  parameters of the coordinated nitrogens. Therefore, similar ENDOR spectra can be simulated if a second imino nitrogen of histidine is assumed instead of the peptide nitrogen. As discussed above, the position of this second histidine ligand would have to depart from “optimal” equatorial position, which leads to a relatively small hfi constant of about 30 MHz. However, it is not clear what happens in such a situation with the hfi parameters of the amino nitrogen in the imidazole ring of this second histidine ligand, as observed in the ESEEM spectrum. Numerical simulations of the ESEEM spectra show that if these amino nitrogen hfi parameters decreased in proportion to the decrease of the hfi constant of

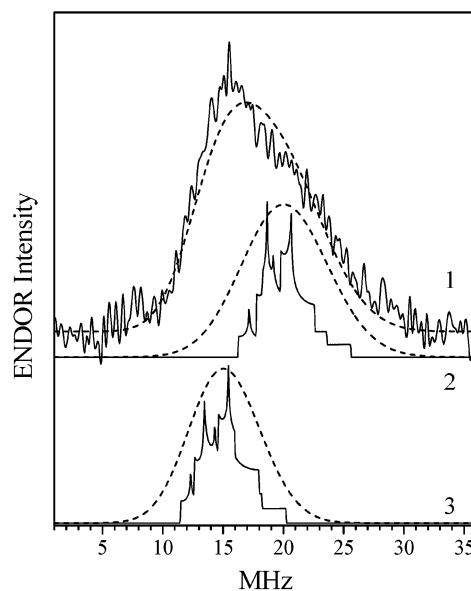


**Figure 6.** Solid trace 1: Davies ENDOR spectrum of surface  $\text{Cu}^{2+}$  centers in *Rb. sphaeroides* (the same as trace 3 in Figure 5). All other traces are simulated numerically. Solid trace 2, simulated for the imidazole imino  $^{14}\text{N}$ :  $a_{\text{iso}} = 40$  MHz,  $T_{\perp} = -3$  MHz,  $k = 2$  MHz, and  $\eta = 0.6$ ; the main axes of the hfi and  $nq_i$  tensors are parallel. Dashed trace 2: simulated for the same hfi parameters, but with  $a_{\text{iso}}$  being Gaussian distributed around the central value of 40 MHz, with the width between the maximal slope points of 12 MHz. Solid trace 3, simulated for the peptide  $^{14}\text{N}$ :  $a_{\text{iso}} = 30$  MHz,  $T_{\perp} = -3$  MHz,  $k = 1.5$  MHz, and  $\eta = 0.75$ ; the main axes of the hfi and  $nq_i$  tensors are parallel. Dashed trace 3: simulated for the same hfi parameters, but with  $a_{\text{iso}}$  being Gaussian distributed around the central value of 30 MHz, with the width between the maximal slope points of 9 MHz. Dashed trace 1 is the sum of dashed traces 2 and 3.

the imino nitrogen (and thus in proportion to the spin density delocalization to the imidazole ring through Cu–N bond), then the presence of such a histidine would be detected in the ESEEM spectra. Therefore, based on the  $\sim 30$  MHz hfi constant necessary to reproduce the  $^{14}\text{N}$  observed in the ENDOR spectrum, we would expect to observe a second remote amino  $^{14}\text{N}$  in the ESEEM spectrum. None was observed. On the other hand, if these hfi parameters become disproportionately small ( $a_{\text{iso}} < 0.5$  MHz and  $T_{\perp} \sim 0.1$  MHz), the resulting ESEEM will be very weak and completely masked by the strong ESEEM from the “normal” histidine ligand.

The fact that our ESEEM data were reasonably explained by a single amino nitrogen from the imidazole ring of the “normal” histidine ligand thus suggests that either the hfi parameters for the amino  $^{14}\text{N}$  of the second histidine are too small to be observed, or the second nitrogen ligand belongs to the peptide group. The first explanation involves at least two coincidences: (i) the hfi constant of the histidine imino nitrogen should become exactly equal to what is expected for an  $sp^3$  hybridization case and (ii) the hfi constant of the amino nitrogen should become small enough as to make this nitrogen unobservable by ESEEM. In addition, the EPR spectra of the surface  $\text{Cu}^{2+}$  center are not indicative of any significant distortions from tetragonal geometry. We therefore consider the second option to be more probable and tentatively assign the second nitrogen to a peptide group.

**3.3. Comparison between Bacterial Species.** Our spectroscopic results indicate that the structures of  $\text{Cu}^{2+}$  surface sites in RCs from *Rb. sphaeroides*, *Rb. capsulatus*, and *Blc. viridis* are similar, and the  $\text{Cu}^{2+}$  ion in these sites has two nitrogen ligands. One of the ligands is an imino nitrogen of histidine

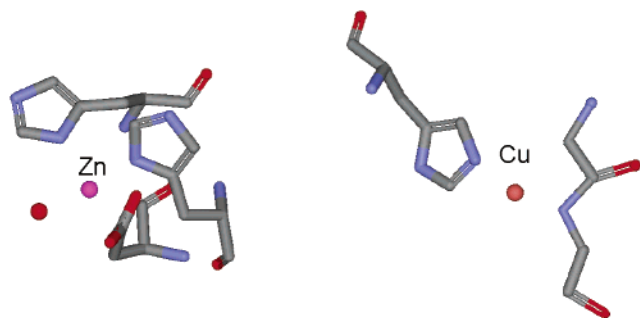


**Figure 7.** Comparison of Zn<sup>2+</sup> and Cu<sup>2+</sup> site structures. (A) The crystallographically determined Zn<sup>2+</sup> site.<sup>55</sup> Zn<sup>2+</sup> is in a tetrahedral environment, coordinated to two His N $\delta$  (H126 and H128), one Asp oxygen (H124), and one water molecule (shown in red). (B) Schematic of a partial Cu<sup>2+</sup> site, determined spectroscopically, to include only one His and one peptide nitrogen. Note that Cu<sup>2+</sup> is shown coordinated to N $\epsilon$  of the histidine, as observed in nearly all type II Cu<sup>2+</sup> centers.<sup>48</sup>

and the other ligand is, most probably, a peptide nitrogen. The conserved nature of the Cu<sup>2+</sup> site structure among different species supports the idea that there might be a native functional role for a RC surface metal site. In each species, the electrochromic response of the bacteriopheophytin cofactors associated with Q<sub>A</sub><sup>-</sup>Q<sub>B</sub>  $\rightarrow$  Q<sub>A</sub>Q<sub>B</sub><sup>-</sup> electron transfer is slowed in the presence of Cu<sup>2+</sup>.<sup>15</sup> Thus, in the species studied to date, there exist structurally analogous Cu<sup>2+</sup> sites that apparently function to modulate electron transfer. It is intuitively unclear, however, why it would be useful to disrupt efficient electron transfer in native systems by metal binding. Interestingly, a similar grouping of four potential histidine ligands is located beneath the Q<sub>B</sub> binding pocket from three different species of structurally characterized RCs from *Rb. sphaeroides*,<sup>1-3</sup> *Blc. viridis*,<sup>45,46</sup> and *Thermochromatium tepidum*.<sup>47</sup> At this point, each surface histidine in the H-subunit region of the RC near Q<sub>B</sub> should be considered a potential ligand for the Cu<sup>2+</sup>.

**3.4. Comparison with the X-ray Data: Mechanistic Implications.** The Cu<sup>2+</sup> spectroscopic results can be compared with the X-ray crystallographic data available for the Zn<sup>2+</sup>, Cd<sup>2+</sup>, Co<sup>2+</sup>, and Ni<sup>2+</sup> coordination sites in bacterial RCs.<sup>18</sup> The crystal structure of *Rb. sphaeroides* RCs shows that Zn<sup>2+</sup> and Cd<sup>2+</sup> are coordinated by the same protein ligands consisting of two histidines, H126 and H128, and an aspartate acid residue, H124.<sup>18</sup> In addition, one water molecule completes the tetrahedral site of Zn<sup>2+</sup>, and three water molecules complete the octahedral coordination sphere of the Cd<sup>2+</sup>. The site is located on the external cytoplasmic side of the RCs, located  $\sim 18$  Å from the Q<sub>B</sub> site and on the H-subunit. Preliminary X-ray diffraction results showed that Co<sup>2+</sup> and Ni<sup>2+</sup> bind to two residues, Asp-M17 and His-H126.<sup>18</sup>

The EPR spectroscopic results thus indicate two notable differences in coordination environments between Cu<sup>2+</sup> and other structurally characterized metal ions at a RC surface site. First, peptide nitrogen coordination, as observed for Cu<sup>2+</sup>, has not been observed in any of the crystallographically determined surface metal site structures (Zn<sup>2+</sup>, Cd<sup>2+</sup>, Co<sup>2+</sup>, and Ni<sup>2+</sup>).<sup>18</sup> Second, definitive evidence for only one imidazole nitrogen bound to the Cu<sup>2+</sup> was observed in the ESEEM spectra. Therefore, it is reasonable to conclude that, in solution, Cu<sup>2+</sup> is binding in a coordination environment that is different from those determined by X-ray crystallography for Zn<sup>2+</sup> and Cd<sup>2+</sup> (Figure 7). Another consideration is N $\delta$  vs N $\epsilon$  histidine coordination at the metal site. In the RC crystal structure, Zn<sup>2+</sup> is bound to the N $\delta$  of the histidines. Unfortunately, the spectroscopic results do not allow us to distinguish between

N $\delta$  and N $\epsilon$  histidine coordination, although nearly all structurally characterized type II Cu centers are coordinated at the N $\epsilon$ .<sup>48</sup>

As discussed above, it is possible that Cu<sup>2+</sup> is coordinated to a second, weakly coupled histidine. Such weak coupling could result from a distorted coordination geometry at the metal site. However, we favor the idea that Cu<sup>2+</sup> is binding to only one histidine as was observed for Co<sup>2+</sup> and Ni<sup>2+</sup> in their respective crystal structures.<sup>18</sup> Like Co<sup>2+</sup> and Ni<sup>2+</sup>, Cu<sup>2+</sup> may bind at essentially the same region on the RC as the Zn<sup>2+</sup> and Cd<sup>2+</sup>, but the coordination geometry may be slightly different due to inherent electronic properties of the metal ion. A surface metal ion binding site might exhibit some flexibility, and thus be able to accommodate different metal ions in their preferable coordination environments. Alternatively, one may speculate that the observed structural differences between the Cu<sup>2+</sup> and other metal ions might be related to the metal sites adapting different structures in frozen solution versus a crystalline environment.

Metal ion specific structural details have thus far been overlooked in the discussion of factors involved in the mechanisms of metal ion modulated electron and proton transfer. Coordination environment differences might explain variations in response of RC electron transfer to Cu<sup>2+</sup> versus Zn<sup>2+</sup> binding. Cu<sup>2+</sup> binding slows Q<sub>A</sub><sup>-</sup>Q<sub>B</sub>  $\rightarrow$  Q<sub>A</sub>Q<sub>B</sub><sup>-</sup> electron transfer to a lesser extent than Zn<sup>2+</sup>, and distributed kinetics are not observed.<sup>12,15</sup> Correlating differences in metal site structure with metal ion specific effects on electron or proton transfer function could provide insight into the mechanism of metal ion modulated electron transfer.

Potentially, different metal site coordination environments might not only influence both structure and flexibility of the surrounding protein matrix,<sup>12,15,19</sup> but also affect electrostatic environments in the RC<sup>16,49</sup> or proton-donating abilities of the coordinated histidine ligands<sup>50,51</sup>—all potential mechanistic factors. For instance, imidazole nitrogen bound to the Cu<sup>2+</sup>, either N $\delta$  or N $\epsilon$  (Figure 1), will be an imino nitrogen, and thus, at neutral pH, an amino imidazole proton<sup>52,53</sup> remains available for donation to Q<sub>B</sub>. Another aspect of metal ion binding is the charge introduced by the metal ion, +2 for Zn and Cu. The main means of neutralizing the charge of the metal ion is with protein side chain ligands. Thus, different ligation could change the effective charge of the metal ion, providing different electrostatic environments that might alter electron or proton transfer.<sup>16,49</sup> As histidine ligands are considered neutral upon metal binding (vs, for instance, cysteines that are deprotonated upon metal binding and contribute  $-1$  charge per ligand), the overall charge on the ligands for Zn is 0, and the charge on the complex is +2.<sup>54</sup> Being at a surface site, Cu<sup>2+</sup>, similar to Zn<sup>2+</sup>, most likely has some open coordination positions that could be occupied by solvent molecules, serving to preserve charge neutrality. For instance, deprotonation of bound water molecules would form OH<sup>-</sup>, neutralizing some of the charge.<sup>54</sup> Different metal ions would be expected to have different pK<sub>a</sub>'s for bound water molecules,<sup>17</sup> and in general, deprotonation equilibria of bound water molecules provide an additional mechanism for the adjustment of the charge at the metal site.<sup>54</sup> Future EPR spectroscopic experiments will be directly aimed at examining the Cu<sup>2+</sup> site for bound solvent molecules.

#### 4. Conclusions

In summary, analogous structural features are observed for the Cu<sup>2+</sup> surface site involved in modulating Q<sub>A</sub><sup>-</sup>Q<sub>B</sub>  $\rightarrow$  Q<sub>A</sub>Q<sub>B</sub><sup>-</sup> electron transfer in RCs from *Rb. sphaeroides*, *Rb. capsulatus*, and *Blc. viridis*. Spectra for each species indicate an intrinsic structural site with one histidine residue and one *sp*<sup>3</sup>-hybridized



(tentatively, peptide) nitrogen as ligands to the  $\text{Cu}^{2+}$ . The solution structure of  $\text{Cu}^{2+}$  is distinct from the coordination environments of the crystallographically determined structures of  $\text{Zn}^{2+}$ ,  $\text{Cd}^{2+}$ , and  $\text{Ni}^{2+}$  bound to the RC surface. These structural differences might be the reason  $\text{Cu}^{2+}$  does not induce the same effect on electron transfer as other metal ions, such as  $\text{Zn}^{2+}$ . Correlating structural features of specific metal ion sites with metal ion induced functional changes might help resolve important mechanistic aspects of metal ion modulated electron transfer.

**Acknowledgment.** This work was supported by the U.S. Department of Energy, Office of Basic Energy Sciences, Division of Chemical Sciences, under Contract No. W-31-109-Eng-38. A.M.R. acknowledges the NSF funding (DBI-9604939) for construction and modification of the pulsed EPR spectrometer used in this work. M.C.T. acknowledges support from ANL.

## References and Notes

- (1) Ermler, U.; Fritzsche, G.; Buchanan, S.; Michel, H. *Structure* **1994**, 2, 925.
- (2) El-Kabbani, O.; Chang, C.-H.; Tiede, D. M.; Norris, J.; Schiffer, M. *Biochemistry* **1991**, 30, 5361.
- (3) Allen, J. P.; Feher, G.; Yeates, T. O.; Komiyama, H.; Rees, D. C. *Proc. Natl. Acad. Sci. U.S.A.* **1988**, 85, 8487.
- (4) Li, J.; Gilroy, D.; Tiede, D. M.; Gunner, M. R. *Biochemistry* **1998**, 37, 2818.
- (5) Mancino, L.; Dean, D.; Blankenship, R. *Biochim. Biophys. Acta* **1984**, 764, 46.
- (6) Tiede, D. M.; Vazquez, J.; Cordova, J.; Marone, P. A. *Biochemistry* **1996**, 35, 10763.
- (7) McPherson, P. H.; Okamura, M. Y.; Feher, G. *Biochim. Biophys. Acta* **1988**, 934, 348.
- (8) Maroti, P.; Wraight, C. A. *Biochim. Biophys. Acta* **1988**, 934, 329.
- (9) Brzezinski, P.; Okamura, M. Y.; Feher, G. Structural Changes Following the Formation of  $\text{D}^+\text{Q}_\text{A}^-$  in Bacterial Reaction Centers: Measurement of Light-induced Electrogenic Events in RCs Incorporated in a Phospholipid Monolayer. In *The Photosynthetic Reaction Center II*; Breton, J., Vermeglio, A., Eds.; Plenum Press: New York, 1992; p 321.
- (10) Graige, M.; Feher, G.; Okamura, M. *Biophys. J.* **1996**, 70, SUAM4.
- (11) Graige, M. S.; Feher, G.; Okamura, M. Y. *Proc. Natl. Acad. Sci. U.S.A.* **1998**, 95, 11679.
- (12) Utschig, L. M.; Ohgashi, Y.; Thurnauer, M. C.; Tiede, D. M. *Biochemistry* **1998**, 37, 8278.
- (13) Paddock, M. L.; Graige, M. S.; Feher, G.; Okamura, M. Y. *Proc. Natl. Acad. Sci. U.S.A.* **1999**, 96, 6183.
- (14) Keller, S.; Beatty, J. T.; Paddock, M.; Breton, J.; Leibl, W. *Biochemistry* **2001**, 40, 429.
- (15) Utschig, L. M.; Poluektov, O.; Schlesselman, S. L.; Thurnauer, M. C.; Tiede, D. M. *Biochemistry* **2001**, 40, 6132.
- (16) Gerencser, L.; Maroti, P. *Biochemistry* **2001**, 40, 1850.
- (17) Adelroth, P.; Paddock, M. L.; Sagle, L. B.; Feher, G.; Okamura, M. Y. *Proc. Natl. Acad. Sci. U.S.A.* **2000**, 97, 13086.
- (18) Axelrod, H. L.; Abresch, E. C.; Paddock, M. L.; Okamura, M. Y.; Feher, G. *Proc. Natl. Acad. Sci. U.S.A.* **2000**, 97, 1542.
- (19) Utschig, L. M.; Poluektov, O.; Tiede, D. M.; Thurnauer, M. C. *Biochemistry* **2000**, 39, 2961.
- (20) Den Blanken, H. J.; Hoff, A. J. *Biochim. Biophys. Acta* **1982**, 681, 365.
- (21) Laible, P. D.; Zhang, Y.; Morris, A. L.; Snyder, S. W.; Ainsworth, C.; Greenfield, S. R.; Wasielewski, M. R.; Parot, P.; Schoepf, B.; Schiffer, M.; Hanson, D. K.; Thurnauer, M. C. *Photosyn. Res.* **1997**, 52, 93.
- (22) Utschig, L. M.; Greenfield, S. R.; Tang, J.; Laible, P. D.; Thurnauer, M. C. *Biochemistry* **1997**, 36, 8548.
- (23) Astashkin, A. V.; Raitsimrin, A. M.; Kennedy, A. R.; Shokhireva, T. K.; Walker, F. A. *J. Phys. Chem. A* **2002**, 106, 74.
- (24) Mims, W. B.; Peisach, J. *J. Chem. Phys.* **1978**, 69, 4921.
- (25) Dikanov, S. A.; Tsvetkov, Y. D. *Electron Spin-Echo Envelope Modulation (ESEEM) Spectroscopy*; CRC Press: Boca Raton, FL, 1992.
- (26) Edmonds, D. T. *Phys. Rep.* **1977**, 29, 233.
- (27) McCracken, J.; Pember, S.; Benkovic, S. J.; Villafranca, J. J.; Miller, R. J.; Peisach, J. *J. Am. Chem. Soc.* **1988**, 110, 1069.
- (28) McCracken, J.; Desai, P. R.; Papadopoulos, N. J.; Villafranca, J. J.; Peisach, J. *Biochemistry* **1988**, 27, 4133.
- (29) Jiang, F.; McCracken, J.; Peisach, J. *J. Am. Chem. Soc.* **1990**, 112, 9035.
- (30) Gurbel, R. J.; Peoples, R.; Doan, P. E.; Cline, J. F.; McCracken, J.; Peisach, J.; Hoffman, B. M.; Valentine, J. S. *Inorg. Chem.* **1993**, 32, 1813.
- (31) Bubacco, L.; Magliozzo, R. S.; Wirt, M. D.; Beltramini, M.; Salvato, B.; Peisach, J. *Biochemistry* **1995**, 34, 1524.
- (32) Elliott, S. J.; Randall, D. W.; Britt, R. D.; Chan, S. I. *J. Am. Chem. Soc.* **1998**, 120, 3247.
- (33) McFadden, D. L.; McPhail, A. T.; Garner, C. D.; Mabbs, F. E. *J. Chem. Soc., Dalton Trans.* **1976**, 47.
- (34) Colaneri, M. J.; Potanza, J. A.; Schugar, H. J.; Peisach, J. *J. Am. Chem. Soc.* **1990**, 112, 9451.
- (35) Dikanov, S. A.; Spoyalov, A. P.; Huttermann, J. *J. Chem. Phys.* **1994**, 100, 7973.
- (36) Van Camp, H. L.; Sands, R. H.; Fee, J. A. *J. Chem. Phys.* **1981**, 75, 2098.
- (37) Polt, R.; Kelly, B. D.; Dangel, B. D.; Tadikonda, U. B.; Ross, R. E.; Raitsimring, A. M.; Astashkin, A. V. *Inorg. Chem.* **2003**, 42, 566.
- (38) Fan, C.; Doan, P. E.; Davoust, C. E.; Hoffman, B. M. *J. Magn. Reson.* **1992**, 98, 62.
- (39) Zhidomirov, G. I.; Schastnev, P. V.; Chuvylkin, N. D. *Quantum-Chemical Calculations of Magnetic Resonance Parameters*; Nauka: Novosibirsk, 1978.
- (40) Iwaizumi, M.; Kudo, T.; Kita, S. *Inorg. Chem.* **1986**, 25, 1546.
- (41) Getz, D.; Silver, B. L. *J. Chem. Phys.* **1974**, 61, 630.
- (42) Ashby, C. I. H.; Cheng, C. P.; Brown, T. L. *J. Am. Chem. Soc.* **1978**, 100, 6057.
- (43) Ashby, C. I. H.; Paton, W. F.; Brown, T. L. *J. Am. Chem. Soc.* **1980**, 102, 2990.
- (44) Roberts, J. E.; Cline, J. F.; Lum, V.; Freeman, H.; Gray, H. B.; Peisach, J.; Reinhammar, B.; Hoffman, B. M. *J. Am. Chem. Soc.* **1984**, 106, 5324.
- (45) Deisenhofer, J.; Epp, O.; Miki, K.; Huber, R.; Michel, H. *J. Mol. Biol.* **1984**, 180, 385.
- (46) Deisenhofer, J.; Epp, O.; Miki, K.; Huber, R.; Michel, H. *Nature* **1985**, 318, 618.
- (47) Nogi, T.; Fathir, I.; Kobayashi, M.; Nozawa, T.; Miki, K. *Proc. Natl. Acad. Sci. U.S.A.* **2000**, 97, 13561.
- (48) Solomon, E. I.; Penfield, K. W.; Wilcox, D. E. Active Sites in Copper Proteins: An Electronic Structure Overview. In *Structure and Bonding*; Springer-Verlag: Berlin, 1983; Vol. 53, p 3.
- (49) Gerencser, L.; Taly, A.; Baciou, L.; Maroti, P.; Sebban, P. *Biochemistry* **2002**, 41, 9132.
- (50) Adelroth, P.; Paddock, M. L.; Tehrani, A.; Beatty, J. T.; Feher, G.; Okamura, M. Y. *Biochemistry* **2001**, 40, 14538.
- (51) Paddock, M.; Sagle, L. B.; Tehrani, A.; Beatty, J. T.; Feher, G.; Okamura, M. Y. *Biochemistry* **2003**, 42, 9626.
- (52) Peisach, J. Pulsed EPR of Copper Proteins. In *Bioinorganic Chemistry of Copper*; Karlin, K. D., Tyeklar, Z., Eds.; Chapman & Hall: New York, 1993; p 21.
- (53) Place, C.; Zimmermann, J.-L.; Mulliez, E.; Guillot, G.; Bois, C.; Chottard, J.-C. *Inorg. Chem.* **1998**, 37, 4030.
- (54) Lippard, S. J.; Berg, J. M. Binding of Metal Ions and Complexes to Biomolecule-Active Centers. In *Principles of Bioinorganic Chemistry*; University Science Books: Mill Valley, 1994; p 218.
- (55) Axelrod, H. L.; Abresch, E. C.; Paddock, M. L.; Okamura, M. Y.; Feher, G. *Proc. Natl. Acad. Sci. U.S.A.* **2000**, 97, 1542.